

Category-Specific Topological Learning of Metal-Organic Frameworks

Dong Chen¹, Chun-Long Chen ^{†2}, and Guo-Wei Wei ^{*1,3,4}

¹*Department of Mathematics, Michigan State University, MI, 48824, USA*

²*Physical Sciences Division, Pacific Northwest National Laboratory, Richland, Washington 99354, United States*

³*Department of Electrical and Computer Engineering, Michigan State University, MI 48824, USA*

⁴*Department of Biochemistry and Molecular Biology, Michigan State University, MI 48824, USA*

Abstract Metal-organic frameworks (MOFs) are porous, crystalline materials with high surface area, adjustable porosity, and structural tunability, making them ideal for diverse applications. However, traditional experimental and computational methods have limited scalability and interpretability, hindering effective exploration of MOF structure-property relationships. To address these challenges, we introduce, for the first time, a category-specific topological learning (CSTL), which combines algebraic topology with chemical insights for robust property prediction. The model represents MOF structures as simplicial complexes and incorporates elemental categorizations to enable balanced, interpretable machine learning study. By integrating category-specific persistent homology, CSTL captures both global and local structural characteristics, rendering multi-dimensional, category-specific descriptors that support a predictive model with high accuracy and robustness across eight MOF datasets, outperforming all previous results. This alignment of topological and chemical features enhances the predictive power and interpretability of CSTL, advancing understanding of structure-property relationships of MOFs and promoting efficient material discovery.

Keywords Persistent homology, Multiscale Topology, Gas selectivity, Diffusivity, Machine learning.

[†]Corresponding author: chunlong.chen@pnnl.gov

^{*}Corresponding author: weig@msu.edu

Contents

1	Introduction	3
2	Results	4
2.1	Workflow and Schematic of a Category-Specific Topological Model	4
2.2	Properties Prediction for MOFs	5
2.3	Feature analysis for the category-specific topological models	7
3	Method	10
3.1	Datasets	10
3.2	Category-Specific Topology	11
3.3	Predictive Modeling	13
A	Evaluation metrics	15
B	Datasets comparison	16
C	Model Repeatability	16
D	Topological objects	17
E	Supplementary tables	19
F	Supplementary figures	20

1 Introduction

Metal-organic frameworks (MOFs) are a unique class of porous materials made up of metal ions or clusters connected to organic ligands, forming crystalline structures with remarkable tunability. Their customizable properties, including high surface area, adjustable porosity, and structural versatility, make MOFs highly suitable for a range of applications [1, 2, 3, 4], such as gas storage[5], separation [6], catalysis [7, 8], and sensing [9]. Although the design possibilities for MOFs are vast, with potentially infinite structures that can be synthesized. A thorough understanding of the relationship between MOF structure and its properties is therefore crucial for designing MOFs tailored to specific applications [10, 11]. However, challenges remain. Traditional experimental methods, while valuable for providing insights into MOF behavior, can be labor-intensive, costly, and limited in scope, hindering the ability to explore the extensive chemical space that MOFs occupy. Computational methods, such as density functional theory (DFT) [12] and molecular dynamics (MD) [13], enable detailed simulations of material behavior but often encounter scalability issues[14]. These methods become computationally prohibitive, particularly for large or complex MOF systems, due to the extensive calculations required [15, 16, 17, 18].

Given the limitations of traditional experimental and computational approaches in studying MOF structure-property relationships, advanced data-driven techniques have become essential. Machine learning (ML) has become increasingly important in studying MOF structure-property relationships and offering a possible solutions to those limitations [19, 20, 21, 22]. And thanks to the high-throughput computational screening, in particular, has emerged as a valuable approach, has laid a solid foundation by generating extensive, high-quality MOF databases[23, 24], such as the CoRE MOF [25] and hMOF datasets [26], which enable ML applications in MOF research. Recently, ML models have leveraged geometric descriptors of MOF structures, such as void fraction and pore volume, to predict gas adsorption properties with notable accuracy [27, 28]. For instance, energy grid histograms have been used as descriptors in ML models to predict gas uptake [29], while other models utilize geometric, atom-type, and chemical feature descriptors to forecast N₂/O₂ selectivity and diffusivity [27]. Despite these advances, prediction accuracy remains a challenge for certain properties. The deep learning (DL) models are introduced, including convolution neural networks, graph neural networks [30, 31] and transformer-based architectures [32, 33, 34, 35], have further enhanced the predictive power for various MOF properties by harnessing large datasets. However, these models come with certain limitations: they can be computationally demanding, often require substantial amounts of data, and sometimes function as 'black-box' systems, presenting challenges for interpretability. Addressing these considerations through continued refinement will help enhance the accessibility and interpretability of ML, particularly in advancing MOF discovery.

To address challenges in MOF research, incorporating mathematically derived, explainable features is essential. These features enhance interpretability and contribute to more robust predictive models for MOF properties. Instead of relying solely on conventional descriptors [27, 28], advanced mathematical tools from fields like geometry and topology can be employed to extract insightful, high-level features. Techniques such as algebraic graph theory [36, 37], persistent homology [38], element-specific persistent homology[39], path topology [40], and topological Laplacians[41] are increasingly used in molecular and materials science, offering new methods to capture the structural and functional nuances of complex materials. Mathematics-based methods have already shown success in fields such as drug discovery[37], biological sciences [42], and materials science [43], linking

structural features to machine learning models for interpretable and detailed representations. For instance, persistent hyperdigraphs have enabled accurate predictions of protein-ligand interactions by capturing essential molecular details within a rigorous mathematical and transformer framework [44]. Mathematical deep learning was a top winner for pose and binding affinity prediction and ranking in D3R Grand Challenges, a worldwide competition series in computer-aided drug design [45, 46].

In this work, we propose a category-specific topological leaning (CSTL) model for predicting the properties of MOFs. This model introduces a mathematically sound and chemically informed framework designed to analyze and predict MOF properties by integrating both structural complexity and elemental composition. Specifically, each MOF structure is represented as a simplicial complex, establishing a robust topological basis for capturing the unique geometric features of MOFs. To enhance structural analysis with chemical insights, the model incorporates category-specific representations by categorizing elements based on valence electron similarity and occurrence frequency. This categorization ensures a balanced representation across the diverse elemental distributions of MOFs. For each elemental category, the model constructs tailored topological representations and applies persistent homology analysis. This method captures both global and local structural features using topological invariants, while also preserving detailed geometric information—particularly beneficial for materials with complex pore networks and spatially organized atomic structures. The model generates multi-dimensional, category-specific descriptors to encapsulate these intricate structural characteristics, which then serve as input to a gradient boosting tree model for predictive analysis. This approach provides an interpretable, chemically informed framework for predicting a broad range of MOF properties, including eight gas selectivity datasets, with the state-of-the-art performance and improved robustness. By aligning topological features with elemental distributions, CSTL addresses the limitations of conventional approaches, advancing the understanding and prediction of structure-property relationships in MOF materials.

2 Results

2.1 Workflow and Schematic of a Category-Specific Topological Model

Figure 1a presents the workflow of our proposed category-specific topological model, designed to analyze and predict properties of MOF structures. In this workflow, the model begins by constructing a simplicial complex representation, which provides a robust topological framework tailored to capture the complex geometry of MOF materials. To enhance this analysis with chemical insights, we introduce category-specific topological representations, defined as categories C_0 through C_7 and C_{all} , where C_{all} encompasses the full structure. As a preprocessing step, an elemental distribution analysis is conducted across the dataset, as illustrated in Figure 1b, highlighting the frequency of elements in the dataset and grouping them by valence electron similarity and occurrence frequency, with distinct colors assigned to each group. Table 1 further specifies these element categories. Notably, the dataset exhibits a broad range of elements, with particular diversity among metallic elements, though specific metallic elements appear less frequently. The categorization process addresses these distribution variances, ensuring that infrequent elements are adequately considered within the predictive model to prevent overemphasis on particular elements’ influence.

Table 1: Element categories for Category-specific topological modeling of MOFs.

Element Category	Notation
Alkali metals, alkaline metals, and other metals	C_0
Transition metals, lanthanoids, actinoids	C_1
Metalloids	C_2
Halogens	C_3
Hydrogen (H)	C_4
Carbon (C)	C_5
Nitrogen (N), Phosphorus (P)	C_6
Oxygen (O), Sulfur (S), Selenium (Se)	C_7
All	C_{all}

Based on these elemental categories, category-specific topological representations are constructed for each MOF structure, employing alpha complexes to provide a categorized-level topology for these materials. Subsequently, category-specific persistent homology analysis is applied, denoted as $H_k^{(a,b)}$, where $k = 0, 1, 2$ represents different topological dimensions, and $a = 0$ to $b = 25$ defines the distance interval, allowing a detailed examination of structure across multiple scales. Multi-dimensional category-specific barcodes are then computed to capture geometric and topological information specific to each elemental category. Following this, a featurization step bins these barcodes into intervals ranging from 0 to 25 Å with a resolution of 0.1 Å, producing length-fixed features from the barcodes. Finally, these features are concatenated to create a comprehensive and category-specific topological descriptor, which is fed into a gradient boosting tree model for predictive modeling across various MOF properties. This approach ensures a balanced representation of elements within the model, enhancing predictive robustness and capturing the nuanced impacts of elemental distribution on MOF properties.

2.2 Properties Prediction for MOFs

In this study, we validated the proposed category-specific topological models by predicting key properties of MOF materials, including the Henry’s constant for N_2 and O_2 (mol/kg/Pa), uptake values for N_2 and O_2 (mol/kg), self-diffusivity of N_2 and O_2 at 1 bar (cm^2/s), and self-diffusivity at infinite dilution (cm^2/s). Table 3 and the Datasets section provide detailed descriptions of these datasets. The prediction outcomes, shown in Figure 2, demonstrate close alignment between predicted and actual values across all eight datasets, with an 80:10:10 random split for training, validation, and testing, respectively[32, 33]. Performance metrics, specifically r^2 and MAE, averaged over 100 repeated experiments, are presented in the top left corner of each dataset’s plot, underscoring the model’s accuracy and reliability.

To benchmark the model’s performance, we compared it with state-of-the-art models, including MOFTransformer[32] and PMTransformer[33], both of which were trained on over a million structures for MOF property prediction. As shown in Table 2, the category-specific topological model consistently outperforms these models across all datasets, achieving superior r^2 , MAE, and RMSE metrics. It is noted that a universal set of hyperparameters was applied across all eight datasets to ensure robustness and prevent overfitting; validation data was not specifically used. In

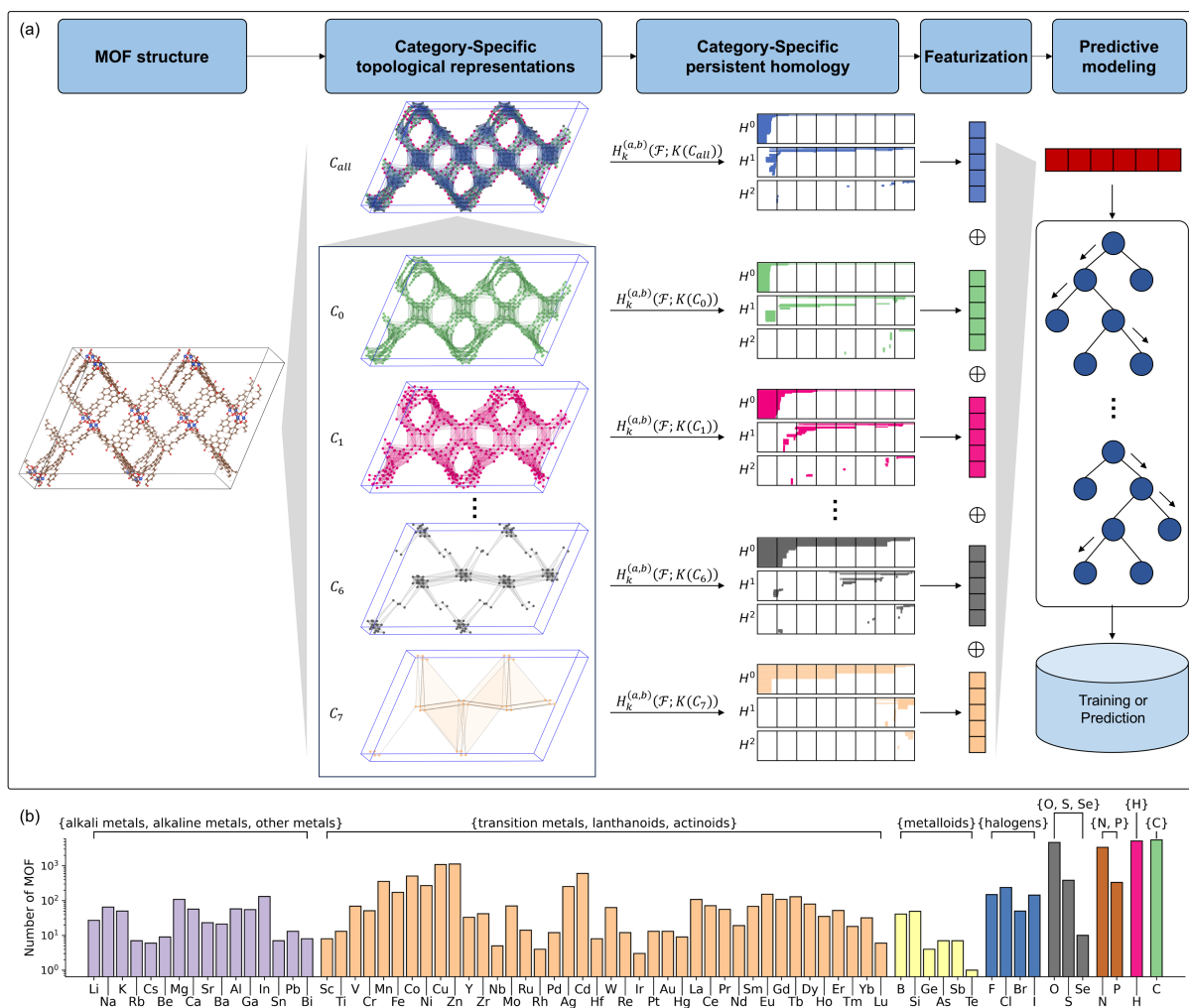


Figure 1: Schematic for Category-Specific Topological Models in MOF Property Prediction. **a** Overview of the category-specific topological models used for predicting properties of MOFs. Given MOF structures (first column), category-specific topological representations are constructed, including a simplicial complex for all structures (C_{all}) and sub-complexes based on categories (C_0 to C_7). The persistent homology method is applied to each category to generate barcode representations. A featurization vector extracts features from these barcodes, which are then used to construct a gradient boosting tree model for predictions on specific datasets. **b** Element distribution across the CoRE MOF v2019 dataset. The y -axis indicates the number of MOFs present in the dataset, with elements categorized based on valence electron similarity and their frequencies in the dataset.

practical applications, incorporating the validation data into the training set could further enhance model accuracy.

Additionally, we evaluated model robustness by testing on a 20% holdout set across all datasets, with results shown in Figure S1 and Table S1, where the proposed model continued to outperform previous models. To ensure the validation stability, we trained 100 models using 10 different seeds, each repeated across 10 randomly initialized predictive models. Heatmaps in Figures S2, S3, and S4 illustrate that variations in seed selection have minimal impact on model performance, confirming the robustness and stability of the predictive model across both fixed and variable data splits.

Table 2: Comparison of CSTL performance with published models across various MOF datasets.

Datasets	CSTL			Descriptor-based[27]		MOFTransformer[32]		PMTransformer[33]
	r2	MAE	RMSE	r2	RMSE	r2	MAE	MAE
Henry’s constant N ₂	0.80	4.90E-07	7.25E-07	0.70	8.94E-07			
Henry’s constant O ₂	0.83	4.98E-07	7.63E-07	0.74	9.60E-07			
N ₂ uptake (mol/kg)	0.79	4.98E-02	7.37E-02	0.71	8.62E-02	0.78	7.10E-02	6.90E-02
O ₂ uptake (mol/kg)	0.85	4.50E-02	6.82E-02	0.74	9.28E-02	0.83	5.10E-02	5.30E-02
Self-diffusion of N ₂ at 1 bar (cm ² /s)	0.80	3.40E-05	4.69E-05	0.76	5.00E-05	0.77	4.52E-05	4.53E-05
Self-diffusion of N ₂ at infinite dilution (cm ² /s)	0.80	3.75E-05	5.15E-05	0.76	5.50E-05			
Self-diffusion of O ₂ at 1 bar (cm ² /s)	0.82	3.21E-05	4.45E-05	0.78	4.98E-05	0.78	4.04E-05	3.99E-05
Self-diffusion of O ₂ at infinite dilution (cm ² /s)	0.79	3.34E-05	4.53E-05	0.74	4.95E-05			

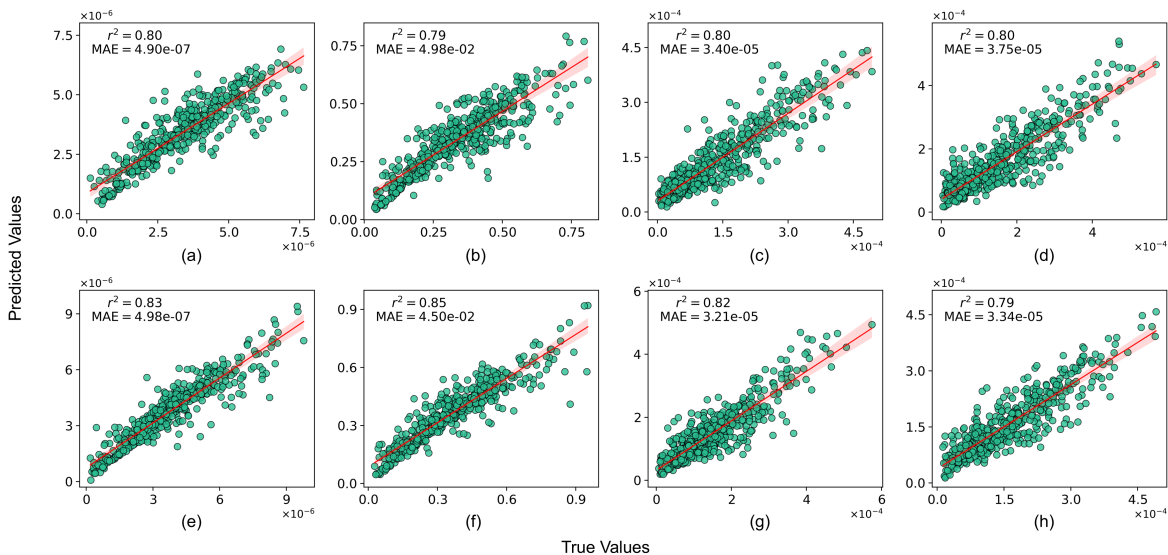


Figure 2: Comparison between predicted and true values for eight datasets on O₂/N₂ selectivity properties in MOF materials. Panels **a-h** show prediction performance for different properties: Henry’s constant for N₂/O₂ (a, e), N₂/O₂ uptake (mol/kg) (b, f), self-diffusivity of N₂/O₂ at 1 bar (cm²/s) (c, g), and self-diffusivity of N₂/O₂ at infinite dilution (cm²/s) (d, h). Each panel displays the R² and the MAE in the upper left corner. Each dataset was randomly split, with 80% used for training, with 10% reserved for testing.

2.3 Feature analysis for the category-specific topological models

In this work, we propose a category-specific topological model to capture the distinctive characteristics of MOF materials. The model encodes each component’s inherent structural and functional attributes by categorizing elements based on their chemical roles and applying persistent homology to analyze each category separately. This approach allows us to represent both the inorganic and organic building blocks of MOFs through distinct topological features, providing a nuanced view that goes beyond treating all atoms as identical.

MOFs are typically built from two primary types of components: inorganic metal nodes and organic linkers. Metal ions or clusters in the inorganic units serve as coordination centers and framework backbones, offering stability and structural rigidity while connecting to the organic linkers. Although metal nodes often appear in smaller quantities than organic atoms, they strongly influence the overall material properties[4, 47]. Because of the diversity among metal elements, it becomes challenging to systematically understand the effect of each metal across all samples—especially for

rare metals like Rn, Bi, and Cs that appear infrequently. Organic linkers, composed mainly of carboxylates or nitrogen-containing ligands, bridge these metal nodes, defining the MOF’s porosity and connectivity. These organic components typically make up the majority of the framework and play a critical role in establishing the intricate, symmetrical structures of MOFs.

To address these component-specific influences, we group metals into categorical types (C_0 , C_1 , C_2 , C_3) while non-metals are clustered into single element or few elements set (C_4 , C_5 , C_6 , and C_7) as shown in Table 1. This CSTL thus captures the functional contributions of distinct components within the MOF without overemphasizing elemental diversity, allowing each category to reveal its unique structural influence through topological embedding.

Visualizing the 2D t-SNE reduction in Figure 3, each green point represents a different MOF material, with distinct clusters reflecting the influence of the CSTL features. Here, key properties such as N_2 uptake, O_2 uptake, and self-diffusivity values are mapped, where materials with the maximum and minimum values for each property are highlighted. Even without predictive modeling, CSTL features differentiate structures with significant property variations, suggesting that the model inherently captures critical structure-property relationships. For example, the MOF material labeled ELOZEK_clean, which has the lowest N_2/O_2 uptake values (8.64e-03 mol/kg for both N_2 and O_2) and Henry’s constants (8.64e-03 mol/kg/Pa for both N_2 and O_2), reflects poor gas absorption. Similarly, COVPAG_clean demonstrates minimal self-diffusivity for N_2 (4.15e-07 cm^2/s), underscoring its limited diffusion capabilities. Such distinctions underscore the power of the CSTL approach to reveal essential structural variations directly through category-specific topological embeddings, distinguishing materials with extreme property values across the MOF dataset.

To quantify the significance of each feature within the proposed CSTL model, we analyzed the tree-based feature importance derived from trained predictive models, as illustrated in Figure 4. This analysis highlights several key trends across different homology dimensions (H_0 , H_1 , and H_2) and categories, reflecting the structural and categorical influence on the model’s predictions.

Generally, we observe that feature importance is concentrated at the beginning of each dimensional homology (H_0 , H_1 , and H_2) across all categories. This is due to the intentionally large end value set for the intervals (25 Å), ensuring the model’s robustness across a broader range of structures, including potential extreme cases beyond the current dataset. Consequently, topological features in the later portion of the interval largely default to zero, explaining the higher importance of features at the beginning of each homology dimension. For category C_2 , which includes metalloids like B, Si, Ge, As, Sb, Te, Po, and At, the feature importance appears limited. Since these elements have valence electron configurations similar to carbon, and their occurrence within the dataset is low (as shown in Figure 1b), their influence is often overshadowed by the predominant presence of carbon. This results in carbon having a stronger impact within this category, affecting the overall model importance distribution.

Focusing on Henry’s constant, shown in the green-highlighted section of Figure 4a, we see distinct variations in feature importance between different gases (N_2 in blue and O_2 in orange). Categories C_5 and C_7 , representing carbon and oxides respectively, exhibit substantial shifts in importance, indicating that carbon-based structures and strongly oxidizing elements influence the selectivity of MOF materials towards these gases. In particular, H_2 in C_5 suggests that carbon-based cavities strongly affect gas selectivity, while H_0 in C_7 highlights the role of oxidizing element spacing on selectivity. A similar trend is observed for N_2 and O_2 uptake properties, as shown in

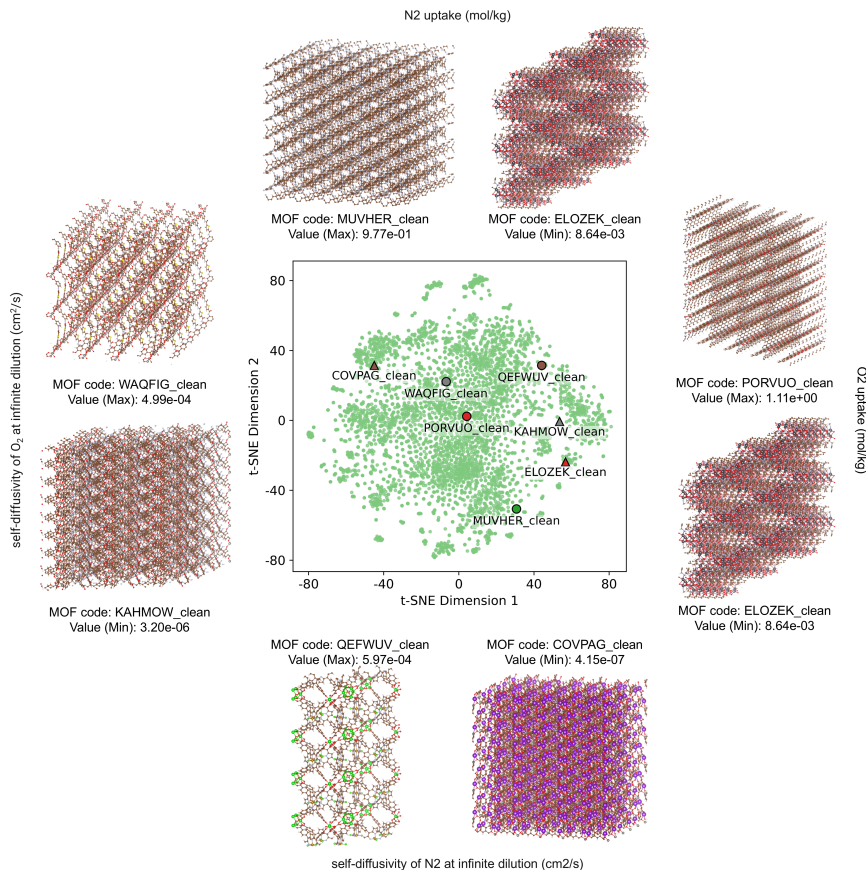


Figure 3: t-SNE feature reduction for category-specific topological features of MOF materials, where each green point represents a distinct MOF material. Highlighted circles and triangles indicate materials with maximum and minimum values, respectively, for four key properties: N_2 uptake (mol/kg), O_2 uptake (mol/kg), self-diffusivity of N_2 at infinite dilution (cm^2/s), and self-diffusivity of O_2 at infinite dilution (cm^2/s). 3D structures of the materials with minimum and maximum values for each property are shown around the t-SNE plot.

Figure 4b. For self-diffusivity of N_2/O_2 , whether at 1 bar or infinite dilution, Figure 4c and d indicate that cycles and cavities within the overall MOF structure, particularly within H_1 and H_2 of the C_{all} category, are the primary factors influencing diffusion properties. This suggests that the model effectively captures the topological elements critical to gas diffusion across MOF structures.

Furthermore, when comparing properties related to gas absorption (Figure 4a and b) and diffusivity (Figure 4c and d), we note that C_1 shows significant variations in importance. This implies that metal atoms have a pronounced effect on gas absorptivity, in contrast to their relatively lower impact on diffusivity properties. In conclusion, this feature analysis demonstrates the versatility and precision of the proposed CSTL model, which adeptly balances generalization and prediction accuracy across diverse property predictions. By integrating both structural and elemental distinctions, the model captures the nuanced interactions within MOF materials, offering a robust framework for predicting many functional properties.

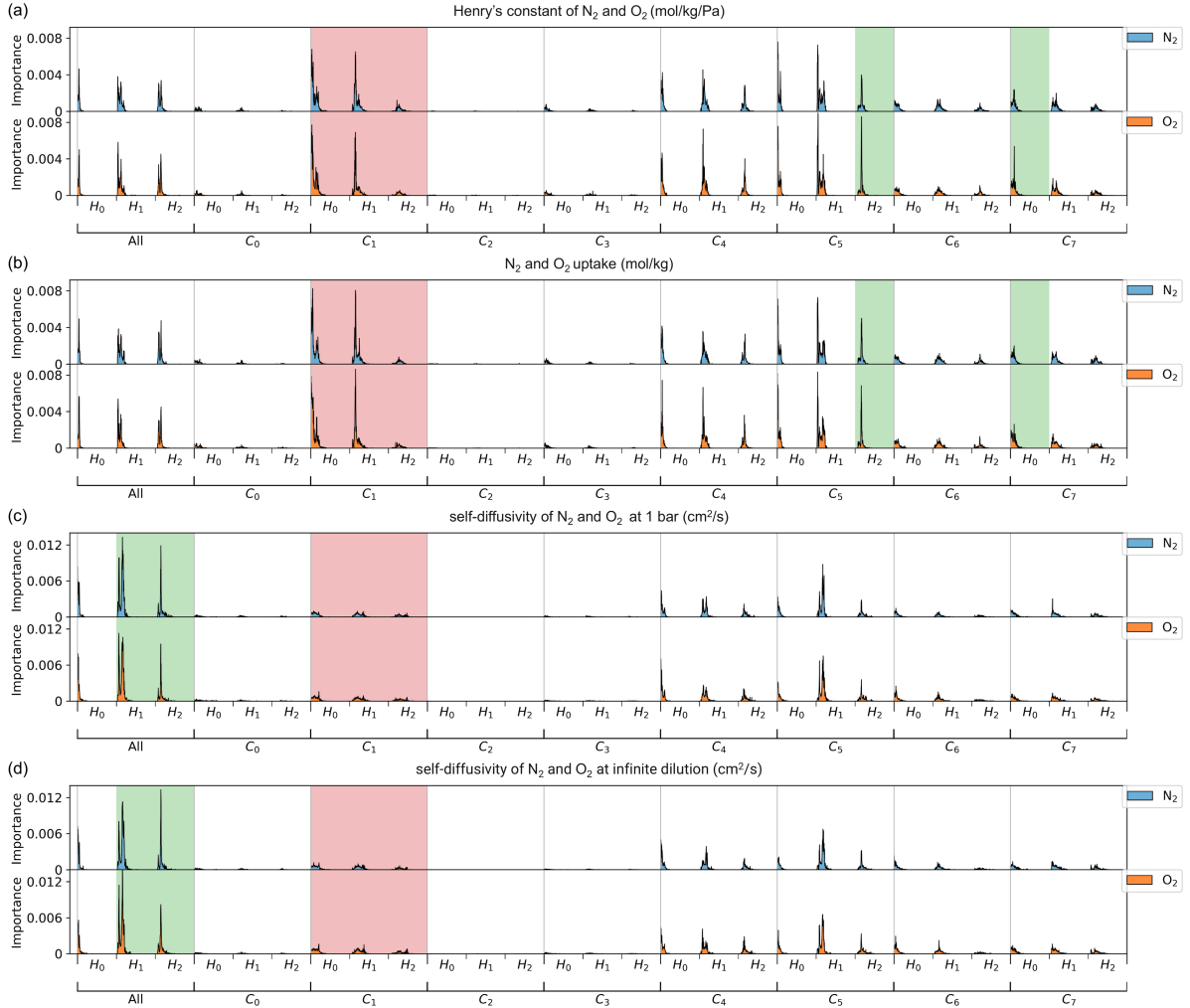


Figure 4: Feature importance analysis for predictive models of eight properties in MOF materials using gradient boosting tree model-based importance. Panels (a)-(d) show the importance of topological features for predicting (a) Henry's constant of N₂ and O₂ (mol/kg/Pa), (b) N₂ and O₂ uptake (mol/kg), (c) self-diffusivity of N₂ and O₂ at 1 bar (cm²/s), and (d) self-diffusivity of N₂ and O₂ at infinite dilution (cm²/s). Each panel presents separate importance values for N₂ (blue) and O₂ (orange) predictions. The bars highlight feature groups by topological dimensions H₀, H₁, and H₂ across different topological categories (C₀ to C₇), with green-shaded regions indicating particularly influential features for different gases (N₂ and O₂) and red-shaded regions indicating particularly influential features across different properties.

3 Method

3.1 Datasets

All datasets used in this study originate from the CoRE MOFs 2019 database [25]. The properties of interest, such as O₂ and N₂ selectivity, were simulated in earlier studies [25]. Certain entries, identified as outliers, were found to lie at the extreme upper end of the distribution, significantly distant from the majority of data points [27]. To enhance the robustness and reliability of the models, these outliers were excluded. Additionally, the data used for validating property predictions was further refined by applying upper-limit threshold values, as outlined in the work

of Orhan et al. [27]. This filtering process removed the outliers, resulting in a more uniform and comprehensive distribution, ensuring a well-represented target-variable space. The filtering methodology follows that of Orhan et al. [27]. To ensure a clear and transparent comparison, we compiled the data information for all methods compared in this study, as summarized in Table S1. In this study, the input features were derived solely from MOF structural data stored in CIF files, without the use of any additional descriptors. Detailed information about the datasets, including the filtered properties and prediction performance, is provided in Table 3.

Table 3: Summary of datasets for N₂ and O₂ selectivity of MOFs.

Datasets (Properties)	Sizes	Train:Valide:Test	Splitting Method
Henry’s constant of N ₂ (mol/kg/Pa)	4744	80:10:10	Random split
Henry’s constant of O ₂ (mol/kg/Pa)	5036	80:10:10	Random split
N ₂ uptake (mol/kg)	5132	80:10:10	Random split
O ₂ uptake (mol/kg)	5241	80:10:10	Random split
self-diffusivity of N ₂ at 1 bar (cm ² /s)	5056	80:10:10	Random split
self-diffusivity of N ₂ at infinite dilution (cm ² /s)	5192	80:10:10	Random split
self-diffusivity of O ₂ at 1 bar (cm ² /s)	5223	80:10:10	Random split
self-diffusivity of O ₂ at infinite dilution (cm ² /s)	5097	80:10:10	Random split

3.2 Category-Specific Topology

Simplicial complex representations Simplicial complexes extend the concept of graphs to higher dimensions, offering richer structural and topological information, as shown an example in Figure 5a. A k -simplex, defined as the convex hull of $k + 1$ independent points, generalizes concepts like points (0-simplex, Figure 5b), line segments (1-simplex, Figure 5c), triangles (2-simplex, Figure 5d), and tetrahedra (3-simplex, Figure 5e). A k -simplex is the k -dimensional analog of these shapes, defined as the convex hull of $k + 1$ affinely independent points, and can be expressed as

$$\sigma^k = \left\{ v \mid v = \sum_{i=0}^k \lambda_i v_i, \sum_{i=0}^k \lambda_i = 1, 0 \leq \lambda_i \leq 1, i = 0, 1, \dots, k \right\}. \quad (1)$$

A simplicial complex K is a collection of simplices such that (1) every face of a simplex in K is also in K , and (2) the intersection of any two simplices is either empty or a common face.

In this work, we represent MOF structures using simplicial complexes, where atoms are 0-simplices (vertices), bonds are 1-simplices (edges), and higher-order interactions, such as atomic rings and cavities, are captured as higher-dimensional simplices. This approach allows us to model not only the pairwise connections but also the higher-order geometric and topological features essential for understanding the physical and chemical properties of MOFs. In the category-specific representation framework for MOF structures, all atoms are grouped into distinct sets based on the categories listed in Table 1, denoted as C_0 to C_7 . Additionally, C_{all} represents the set containing all atoms. For each category-specific set, topological representations are constructed to capture the interactions among atoms across different categories.

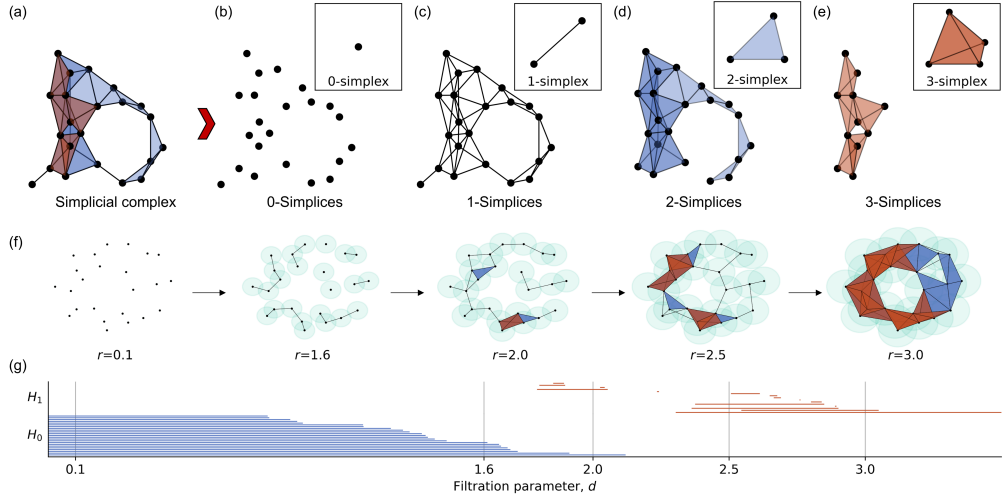


Figure 5: Illustration of concepts in persistent homology. (a) An example of a simplicial complex. (b)-(e) Expansion of the simplicial complex in (a) into different simplex dimensions: (b) 0-simplices (vertices), with the 0-simplex as a building block shown in the upper right; (c) 1-simplices (edges), with the 1-simplex in the upper right; (d) 2-simplices (triangles), with the 2-simplex in the upper right; and (e) 3-simplices (tetrahedron), with the 3-simplex in the upper right. (f) A nested simplicial complex with an increasing parameter r , exemplifying an alpha complex. (g) Barcode representation of H_0 and H_1 for the complex in (f), with specific values of $r = 0.1, 1.6, 2.0, 2.5,$ and 3.0 corresponding to the simplicial complex states shown in (f).

Homology and persistent homology To analyze the topological properties of MOF structures represented by simplicial complexes, homology is used as an algebraic tool. By employing concepts such as chains, chain groups, and boundary operators, homology groups capture features like connected components, loops, and cavities within the material. For a given dimension k , the k -chain group C_k is formed by k -simplices with coefficients from a specified field (e.g., \mathbb{Z}_2). The boundary operator ∂_k maps k -chains to $(k - 1)$ -chains, defined as:

$$\partial_k[v_0, v_1, \dots, v_k] = \sum_{i=0}^k (-1)^i [v_0, \dots, \hat{v}_i, \dots, v_k], \quad (2)$$

where \hat{v}_i indicates the omission of vertex v_i . This operation helps identify cycles (chains with no boundary) and boundaries (chains that are boundaries of higher-dimensional simplices). The k -th homology group H_k is then defined as:

$$H_k = \text{Ker}(\partial_k) / \text{Im}(\partial_{k+1}), \quad (3)$$

which represents k -dimensional holes, such as connected components (H_0), loops (H_1), and voids (H_2) in the MOF structure. The homology group (H) allows for the measurement of topological features, such as Betti numbers (β), which count the number of independent k -dimensional cycles, reflecting the number of k -dimensional holes. They can be calculated by, $\beta_k = \text{rank}(H_k) = \text{rank}(Z_k) - \text{rank}(B_k)$.

To capture how these topological features vary with the spatial scale, persistent homology is introduced [48, 49, 38]. It tracks the evolution of homological features as a parameter (e.g., bond length or distance threshold) changes. This is achieved through a filtration, a sequence of nested

subcomplexes $\{K_i\}$ where $K_0 \subseteq K_1 \subseteq \dots \subseteq K_n$. There are some common used filtration methods, such Vietoris-Rips complex [50], Čech complex [51], and alpha complex [52]. In this work, we employ the alpha complex for analyzing MOF structures. The alpha complex is constructed based on the Delaunay triangulation of the atomic positions. For a given parameter α , a simplex (e.g., an edge, triangle, or tetrahedron) is included in the complex if the radius of the smallest empty circumsphere that encloses it is less than or equal to α . As α increases, the alpha complex grows, progressively capturing larger topological features in the MOF structure, such as rings, tunnels, and cavities, an example is shown Figure 5f.

Persistent homology quantifies the persistence of these features across different scales, revealing stable patterns that correspond to critical geometric and chemical properties of the MOF. Each k -th homology group is tracked across the filtration, providing insights into how certain features (e.g., porosity or connectivity) appear, merge, and disappear as the structure evolves. These persistent patterns are typically visualized using barcodes [53], where the length of each bar represents the lifespan of a particular topological feature. An example of barcodes with corresponding alpha complex is shown in Figure 5g.

Category-Specific topological embedding Persistent homology does not distinguish different element types and thus gives a poor representation for chemical and biological systems. Element-specific persistent homology was introduced to better capture chemical and biological properties [39]. In this work, we propose a category-specific topological embedding approach to preserve the chemical and physical information inherent in MOF structures. Elements in the periodic table are categorized into eight distinct groups based on their chemical similarities and structural roles (see Table 1). Before constructing the embeddings, the supercell of each material is scaled uniformly to approximately $64 \text{ \AA} \times 64 \text{ \AA} \times 64 \text{ \AA}$ to ensure that the topological analysis is performed consistently across different structures.

Our method involves two main stages: (1) For a given MOF structure, category-specific topological representations are constructed based on the elemental types of atoms, categorized as C_0 to C_7 , along with an additional set C_{all} containing all atoms. (2) The persistent homology of each category from stage (1) is computed to capture global and category-level topological patterns, characterized by their Betti numbers in the H_0 , H_1 , and H_2 homology spaces. This approach allows the topological analysis to incorporate both structural and chemical information. For each category and each homology dimension, we employ a grid-based method to generate the topological embeddings. Specifically, we construct a grid ranging from 0 to 25 \AA with a step size of 0.1 \AA and record the Betti numbers (i.e., the number of topological features that persist at each scale). This process yields a feature vector of length 750 ($250 \text{ steps} \times 3 \text{ homology dimensions: } H_0, H_1, \text{ and } H_2$) for each element category. By concatenating these feature vectors across all eight categories, we obtain a 6000-dimensional representation. When combined with the features derived from the entire MOF structure, the final topological embedding results in a 6750-dimensional vector that integrates both global structural patterns and category-specific chemical information.

3.3 Predictive Modeling

In this work, a Gradient Boosting Tree (GBT) model was constructed to perform regression analysis using the proposed category-specific topological embedding as input features. Gra-

gradient boosting is an ensemble learning method that builds multiple weak learners (typically decision trees) sequentially, where each tree is trained to correct the errors made by the previous ones, thereby producing a more accurate model. We implemented the gradient boosting regressor from Scikit-learn [54], optimizing the squared error loss function. The model parameters were set as follows: `max_depth=7`, `max_features='sqrt'`, `min_samples_leaf=1`, `min_samples_split=2`, `n_estimators=10,000`, and `subsample=0.5`. These settings were not fine-tuned, as we aimed to demonstrate the robustness of the proposed predictive model with a single set of hyperparameters.

All input features were normalized using standard scaling, and the target properties were standardized to facilitate regression analysis. For model evaluation, we split the dataset into train, validation, and test sets using an 80%, 10%, and 10% ratio, respectively [32, 27]. Since we used a universal set of hyperparameters, the validation set was not employed for model selection. Instead, 80% of the data was used for training to establish a fair comparison with previous works. The results for the test set (10%) and for both the test and validation sets combined (20%) are reported to assess the model's performance comprehensively.

To ensure robust evaluation, we repeated the random data split 10 times, and for each split, 10 models were trained with different random seeds, resulting in a total of 100 models per dataset. The performance metrics, including root mean square error (RMSE), mean absolute error (MAE), and r^2 correlation, were averaged over these 100 models and reported as the final results (as seen in Supplementary Information Section 1). This approach of using a single set of hyperparameters and a consistent evaluation protocol highlights the robustness of the predictive model, making the results reliable and comparable to existing methods in the literature.

Data availability

The datasets utilized in this work are derived from the structures available in the CoRE MOFs 2019 database [25]. The properties for each dataset were obtained using the methods outlined in Orhan et al. [27].

Acknowledgments

This work was supported in part by NIH grants R01GM126189, R01AI164266, and R35GM148196, National Science Foundation grants DMS2052983 and IIS-1900473, Michigan State University Research Foundation, and Bristol-Myers Squibb 65109. C.-L.C. gratefully acknowledges financial support from the Defense Threat Reduction Agency (Project CB11141), and the Department of Energy (DOE), Office of Science, Office of Basic Energy Sciences (BES) under an award FWP 80124 at Pacific Northwest National Laboratory (PNNL). PNNL is a multiprogram national laboratory operated for the Department of Energy by Battelle under Contract DE-AC05-76RL01830.

A Evaluation metrics

In this work, the Root Mean Square Error (RMSE), Mean Absolute Error (MAE), and R^2 (Coefficient of Determination) were used for evaluating machine learning models.

The Root Mean Square Error (RMSE) is a standard way to measure the error of a model in predicting quantitative data. It quantifies the difference between the predicted values (\hat{y}_i) and the true values (y_i). The formula for RMSE is defined as:

$$\text{RMSE} = \sqrt{\frac{1}{n} \sum_{i=1}^n (\hat{y}_i - y_i)^2} \quad (4)$$

where: 1) n is the number of observations. 2) \hat{y}_i is the predicted value for the i -th observation. 3) y_i is the actual value for the i -th observation. 4) Lower values of RMSE indicate a better fit of the model to the data. It has the same unit as the response variable.

The Mean Absolute Error (MAE) measures the average magnitude of errors in a set of predictions, without considering their direction. It calculates the average of the absolute differences between predicted and actual values. The formula for MAE is given by:

$$\text{MAE} = \frac{1}{n} \sum_{i=1}^n |\hat{y}_i - y_i| \quad (5)$$

where: 1) n is the number of observations. 2) \hat{y}_i is the predicted value for the i -th observation. 3) y_i is the actual value for the i -th observation. 4) MAE provides a straightforward interpretation of the average error. Like RMSE, lower values indicate a better fit, and it has the same unit as the response variable.

The Coefficient of Determination (R^2) measures the proportion of variance in the dependent variable that is predictable from the independent variables. It essentially indicates how well the model fits the data. The R^2 value ranges from 0 to 1, with 1 indicating a perfect fit. The formula for R^2 is defined as:

$$R^2 = 1 - \frac{\sum_{i=1}^n (y_i - \hat{y}_i)^2}{\sum_{i=1}^n (y_i - \bar{y})^2} \quad (6)$$

where: 1) n is the number of observations. 2) y_i is the actual value for the i -th observation. 3) \hat{y}_i is the predicted value for the i -th observation. 4) \bar{y} is the mean of the observed values. 5) An R^2 value close to 1 means that the model explains a large portion of the variance, whereas a value close to 0 indicates that the model explains very little variance.

B Datasets comparison

In this work, we compared the proposed method with the descriptor-based method [27], MOF-Transformer [32], and PMTransformer [33]. Although the eight datasets listed in Table 2 are derived from the study by Orhan et al. [27], their sizes differ slightly. The datasets used in this work were directly generated from the source repository (<https://github.com/ibarisorhan/MOF-O2N2/tree/main/mofScripts>) established by Orhan et al. [27]. While the datasets used in MOF-Transformer [32] and PMTransformer [33] were also obtained from the same source, their exact data details were not explicitly provided. To ensure a clear and transparent comparison, we compiled the data information for all methods compared in this study, as summarized in Table 4.

Table 4: Comparison of datasets used in the published works across various MOF datasets.

Datasets	CSTL	Descriptor-based[27]	MOFTransformer[32]	PMTransformer[33]
Henry’s constant N ₂	4744	4755		
Henry’s constant O ₂	5036	5045		
N ₂ uptake (mol/kg)	5132	5158	5286	5286
O ₂ uptake (mol/kg)	5241	5259	5286	5286
Self-diffusion of N ₂ at 1 bar (cm ² /s)	5056	5079	5286	5286
Self-diffusion of N ₂ at infinite dilution (cm ² /s)	5192	5202		
Self-diffusion of O ₂ at 1 bar (cm ² /s)	5223	5247	5286	5286
Self-diffusion of O ₂ at infinite dilution (cm ² /s)	5097	5115		

C Model Repeatability

To ensure robust evaluation, we repeated the random data split 10 times, and for each split, 10 models were trained with different random seeds, resulting in a total of 100 models per dataset. The performance metrics, including RMSE, MAE, and r^2 correlation, were averaged over these 100 models and reported as the final results. This approach of using a single set of hyperparameters and a consistent evaluation protocol highlights the robustness of the predictive model, making the results reliable and comparable to existing methods in the literature. Specifically, the Gradient Boosting Tree (GBT) model was constructed to perform regression analysis using the proposed category-specific topological learning (CSTL) embedding as input features. We implemented the gradient boosting regressor from Scikit-learn [54], optimizing the squared error loss function. The model parameters were set as follows: `max_depth=7`, `max_features='sqrt'`, `min_samples_leaf=1`, `min_samples_split=2`, `n_estimators=10,000`, and `subsample=0.5`. The heatmap of MAE/ r^2 /RMSE values for 100 predictive models across eight datasets are shown in Figure 7, Figure 8, and Figure 9.

D Topological objects

Graph. The graph is a key structure for illustrating relationships among different entities, representing one of the most prevalent data forms. It is composed of nodes (or vertices) and edges, which establish the connections between these nodes. Graphs can be enhanced in several ways, such as by adding directionality to create directed graphs (digraph), assigning weights for weighted graphs, or incorporating geometric properties in geometric graphs. These enhanced graphs are excellent for representing relationships and attributes in various scenarios. Formally, a graph is defined as a pair (V, E) , where V represents a set of vertices and E , a subset of $V \times V$, signifies the set of edges. Vertices and edges are the core components of a graph. Tools like adjacency matrices, degree matrices, and Laplacian matrices are utilized to describe the interactions between vertices and edges. These matrices are pivotal in graph theory and network analysis, capturing the graph's underlying topological structure. Although graphs are inherently one-dimensional, methods from simplicial complexes are sometimes used to express the graph's higher-dimensional aspects.

Simplicial complex. A simplicial complex is a type of topological space constructed from basic units known as simplices. A simplex extends the notion of a triangle or tetrahedron to any number of dimensions. For a set of vertices V , a k -simplex σ_k is typically represented by a subset of V containing $k + 1$ elements, and is expressed as $\sigma = \langle v_0, v_1, \dots, v_k \rangle$. Any subset of σ_{k-1} is considered a face of σ_k .

A *simplicial complex*, denoted as K , based on a vertex set V , is defined by a group of simplices that meet two criteria: (1) If a simplex σ is part of K , then all of its faces, including individual vertices, are also included in K ; (2) The intersection of any two simplices within K is either empty or a face (subset) common to both simplices. From these characteristics, it's evident that a graph can be interpreted as a 1-dimensional simplicial complex, where its simplices consist of vertices (0-simplices) and edges (1-simplices).

In a k -simplex, the boundary is the set of its $(k - 1)$ -dimensional faces. The *boundary operator*, symbolized as ∂_k , operates on a k -simplex $\langle v_0, v_1, \dots, v_k \rangle$ in the following mathematical form:

$$\partial_k \langle v_0, v_1, \dots, v_k \rangle = \sum_{i=0}^k (-1)^i \langle v_0, \dots, \widehat{v}_i, \dots, v_k \rangle, \quad (7)$$

where \widehat{v}_i indicates the exclusion of the vertex v_i . A chain complex is a series of Abelian groups (or modules), interconnected by boundary operators. Suppose G is an Abelian group. The k -th group in the chain complex, denoted as $C_k(K; G)$, comprises formal sums of k -simplices. The boundary operator $\partial_k : C_k(K; G) \rightarrow C_{k-1}(K; G)$ maps a k -simplex to its $(k - 1)$ -dimensional boundary. The sequence of the chain complex can be represented as:

$$\dots \xrightarrow{\partial_{k+1}} C_k(K; G) \xrightarrow{\partial_k} C_{k-1}(K; G) \xrightarrow{\partial_{k-1}} \dots \xrightarrow{\partial_2} C_1(K; G) \xrightarrow{\partial_1} C_0(K; G). \quad (8)$$

A critical characteristic of the boundary operator is that the composition of two consecutive boundary operators equals zero, i.e., $\partial_{k-1} \circ \partial_k = 0$. This implies that the boundary of a boundary is always null, carrying significant topological implications. The structure of the chain complex provides a systematic way to analyze how boundaries integrate with each other. Beyond the simplicial complex, other topological objects—such as the clique complex, cell complex, cellular sheaf [55],

hypergraph, neighborhood complex [56, 57], Hom complex, knot, link, and tangle [58, 59]—can be further explored in the analysis of the given data.

E Supplementary tables

In the following section, we provide supplementary tables that offer additional data and insights pertinent to our study. Readers are encouraged to refer to these tables for a more detailed exploration of the topics covered in the main text.

Table 5: Comparison of CSTL models with different training-test splits.

Datasets	CSTL(80% training, 10% test)			CSTL(80% training, 20% test)		
	r^2	mae	rmse	r^2	mae	rmse
Henry's constant N ₂	0.80	4.90E-07	7.25E-07	0.79	4.98E-07	7.36E-07
Henry's constant O ₂	0.83	4.98E-07	7.63E-07	0.83	5.00E-07	7.69E-07
N ₂ uptake (mol/kg)	0.79	4.98E-02	7.37E-02	0.79	4.98E-02	7.39E-02
O ₂ uptake (mol/kg)	0.85	4.50E-02	6.82E-02	0.85	4.54E-02	6.90E-02
Self-diffusion of N ₂ at 1 bar (cm ² /s)	0.80	3.40E-05	4.69E-05	0.80	3.39E-05	4.64E-05
Self-diffusion of N ₂ at infinite dilution (cm ² /s)	0.80	3.75E-05	5.15E-05	0.80	3.79E-05	5.21E-05
Self-diffusion of O ₂ at 1 bar (cm ² /s)	0.82	3.21E-05	4.45E-05	0.81	3.32E-05	4.62E-05
Self-diffusion of O ₂ at infinite dilution (cm ² /s)	0.79	3.34E-05	4.53E-05	0.79	3.35E-05	4.54E-05

F Supplementary figures

In this section, we present a series of supplementary figures that further elucidate and complement the findings discussed in the main text. Readers are encouraged to consult these figures for a richer understanding and visual representation of the concepts and results introduced in the main manuscript.

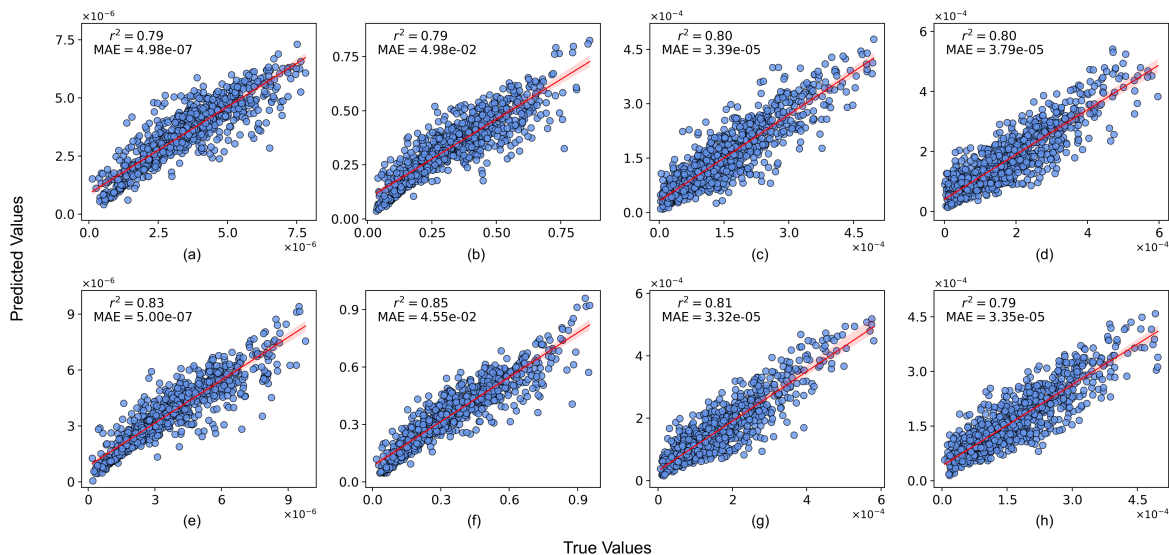


Figure 6: Comparison between predicted and true values for eight datasets on O_2/N_2 selectivity properties in MOF materials. Panels **a-h** show prediction performance for different properties: Henry's constant for N_2/O_2 (a, e), N_2/O_2 uptake (mol/kg) (b, f), self-diffusivity of N_2/O_2 at 1 bar (cm^2/s) (c, g), and self-diffusivity of N_2/O_2 at infinite dilution (cm^2/s) (d, h). Each panel displays the R^2 and the MAE in the upper left corner. Each dataset was randomly split, with 80% used for training and rest 20% for testing.

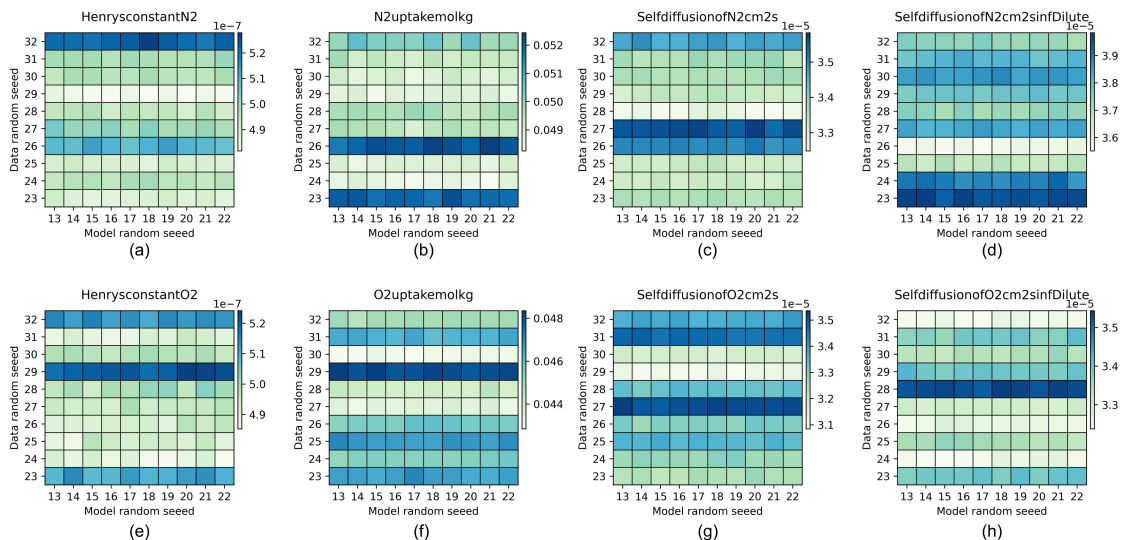


Figure 7: Heatmap of MAE values for predictive models across eight datasets related to O_2/N_2 selectivity properties in MOF materials. Panels (a)-(h) represent the MAE results for properties including Henry's constant for N_2 (a) and O_2 (e), N_2/O_2 uptake (mol/kg) for N_2 (b) and O_2 (f), self-diffusivity at 1 bar (cm^2/s) for N_2 (c) and O_2 (g), and self-diffusivity at infinite dilution (cm^2/s) for N_2 (d) and O_2 (h). Each dataset was randomly split 10 times with seeds ranging from 23 to 32, reserving 80% for training and 10% for testing. For each split, 10 separate models were trained with random seeds from 13 to 22, resulting in a total of 100 models per dataset. The heatmap color bar illustrates the MAE values for these 100 models, providing insight into prediction variability across different datasets and modeling scenarios.

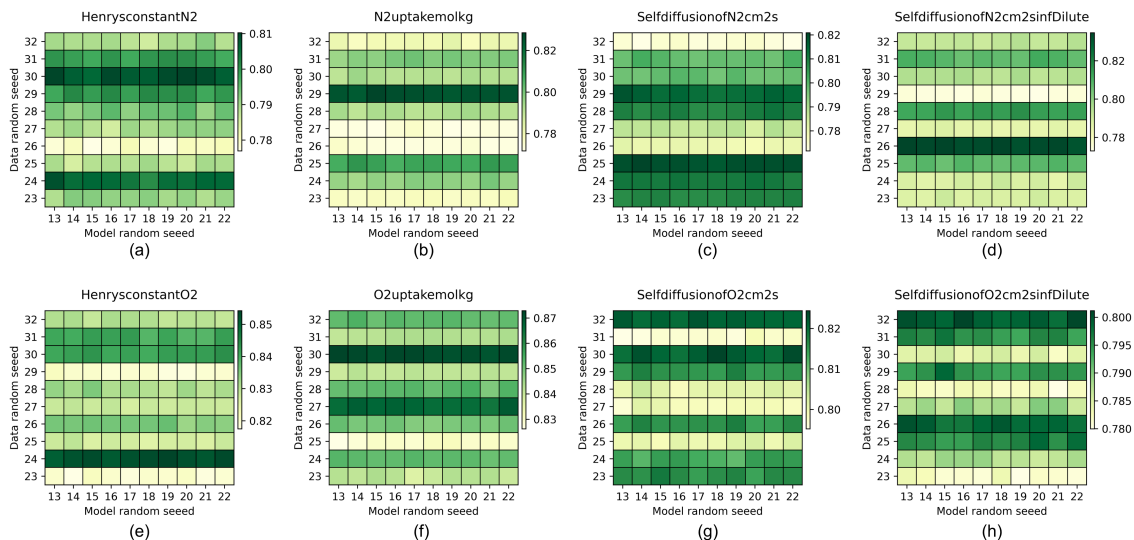


Figure 8: Heatmap of r^2 values for predictive models across eight datasets related to O_2/N_2 selectivity properties in MOF materials. Panels (a)-(h) represent the MAE results for properties including Henry's constant for N_2 (a) and O_2 (e), N_2/O_2 uptake (mol/kg) for N_2 (b) and O_2 (f), self-diffusivity at 1 bar (cm^2/s) for N_2 (c) and O_2 (g), and self-diffusivity at infinite dilution (cm^2/s) for N_2 (d) and O_2 (h). Each dataset was randomly split 10 times with seeds ranging from 23 to 32, reserving 80% for training and 10% for testing. For each split, 10 separate models were trained with random seeds from 13 to 22, resulting in a total of 100 models per dataset. The heatmap color bar illustrates the r^2 values for these 100 models.

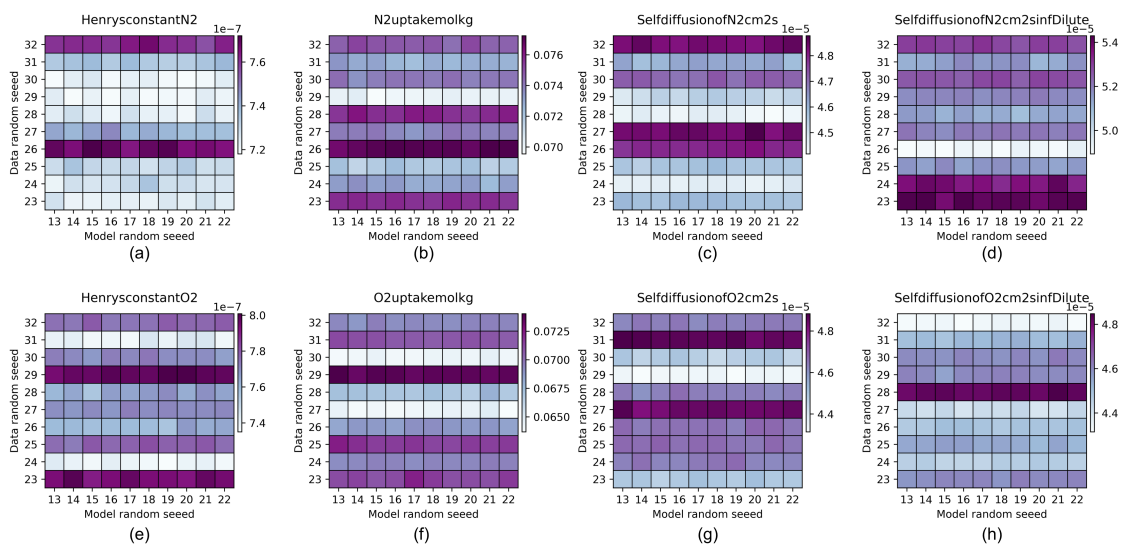


Figure 9: Heatmap of RMSE values for predictive models across eight datasets related to O_2/N_2 selectivity properties in MOF materials. Panels (a)-(h) represent the MAE results for properties including Henry's constant for N_2 (a) and O_2 (e), N_2/O_2 uptake (mol/kg) for N_2 (b) and O_2 (f), self-diffusivity at 1 bar (cm^2/s) for N_2 (c) and O_2 (g), and self-diffusivity at infinite dilution (cm^2/s) for N_2 (d) and O_2 (h). Each dataset was randomly split 10 times with seeds ranging from 23 to 32, reserving 80% for training and 10% for testing. For each split, 10 separate models were trained with random seeds from 13 to 22, resulting in a total of 100 models per dataset. The heatmap color bar illustrates the RMSE values for these 100 models.

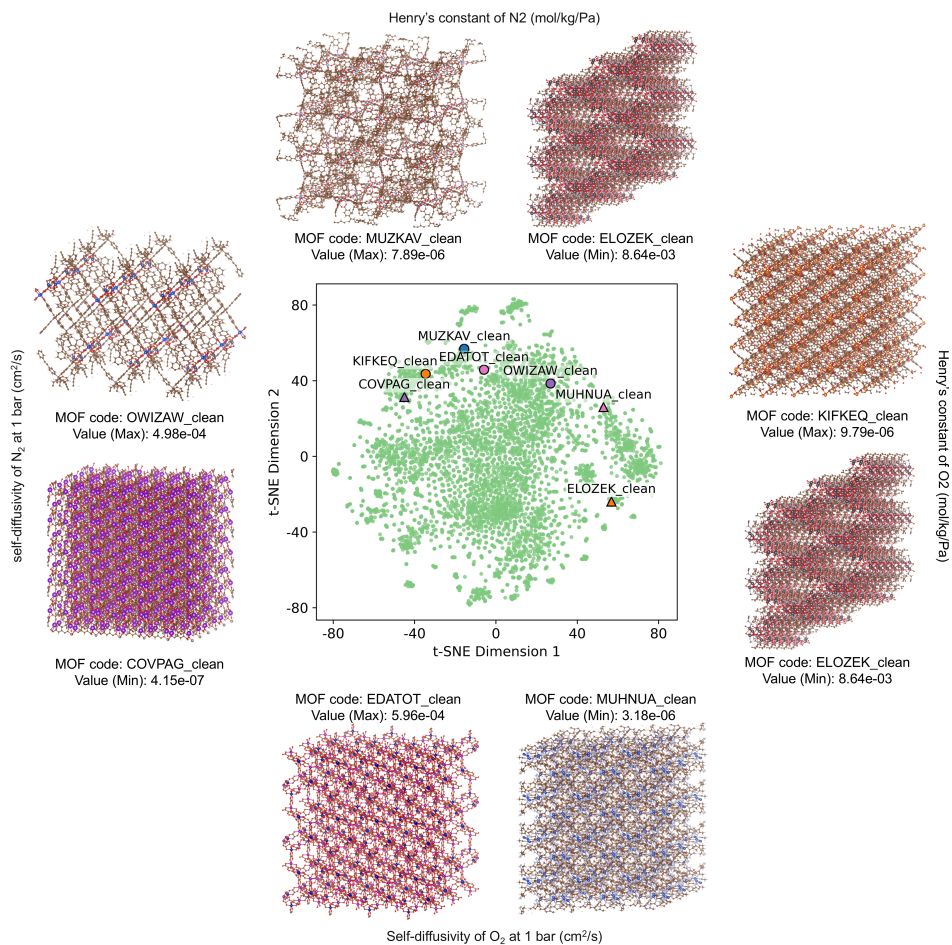


Figure 10: t-SNE feature reduction for category-specific topological features of MOF materials, where each green point represents a distinct MOF material. Highlighted circles and triangles indicate materials with maximum and minimum values, respectively, for four key properties: Henry's constant for N₂, Henry's constant for O₂, self-diffusivity of N₂ at 1 bar (cm²/s), and self-diffusivity of O₂ at 1 bar (cm²/s). 3D structures of the materials with minimum and maximum values for each property are shown around the t-SNE plot.

References

- [1] Ralph Freund, Orysia Zaremba, Giel Arnauts, Rob Ameloot, Grigorii Skorupskii, Mircea Dincă, Anastasiya Bavykina, Jorge Gascon, Aleksander Ejsmont, Joanna Goscianska, et al. The current status of mof and cof applications. *Angewandte Chemie International Edition*, 60(45):23975–24001, 2021.
- [2] Sandeep Kumar, Shikha Jain, Monika Nehra, Neeraj Dilbaghi, Giovanna Marrazza, and Ki-Hyun Kim. Green synthesis of metal–organic frameworks: A state-of-the-art review of potential environmental and medical applications. *Coordination Chemistry Reviews*, 420:213407, 2020.
- [3] Chun-Long Chen and Alicia M Beatty. Guest inclusion and structural dynamics in 2-d hydrogen-bonded metal- organic frameworks. *Journal of the American Chemical Society*, 130(51):17222–17223, 2008.
- [4] Chun-Long Chen, Andrea M Goforth, Mark D Smith, Cheng-Yong Su, and Hans-Conrad zur Loye. [co₂ (ppca) 2 (h₂o)(v4o12) 0.5]: a framework material exhibiting reversible shrinkage and expansion through a single-crystal-to-single-crystal transformation involving a change in the cobalt coordination environment. *Angewandte Chemie International Edition*, 44(41):6673–6677, 2005.
- [5] Shengqian Ma and Hong-Cai Zhou. Gas storage in porous metal–organic frameworks for clean energy applications. *Chemical Communications*, 46(1):44–53, 2010.
- [6] Qihui Qian, Patrick A Asinger, Moon Joo Lee, Gang Han, Katherine Mizrahi Rodriguez, Sharon Lin, Francesco M Benedetti, Albert X Wu, Won Seok Chi, and Zachary P Smith. Mof-based membranes for gas separations. *Chemical reviews*, 120(16):8161–8266, 2020.
- [7] JeongYong Lee, Omar K Farha, John Roberts, Karl A Scheidt, SonBinh T Nguyen, and Joseph T Hupp. Metal–organic framework materials as catalysts. *Chemical Society Reviews*, 38(5):1450–1459, 2009.
- [8] Kent O Kirlikovali, Zhijie Chen, Timur Islamoglu, Joseph T Hupp, and Omar K Farha. Zirconium-based metal–organic frameworks for the catalytic hydrolysis of organophosphorus nerve agents. *ACS applied materials & interfaces*, 12(13):14702–14720, 2020.
- [9] Lauren E Kreno, Kirsty Leong, Omar K Farha, Mark Allendorf, Richard P Van Duyne, and Joseph T Hupp. Metal–organic framework materials as chemical sensors. *Chemical reviews*, 112(2):1105–1125, 2012.
- [10] Yamil J Colón and Randall Q Snurr. High-throughput computational screening of metal–organic frameworks. *Chemical Society Reviews*, 43(16):5735–5749, 2014.
- [11] Sangwon Lee, Baekjun Kim, Hyun Cho, Hooseung Lee, Sarah Yunmi Lee, Eun Seon Cho, and Jihan Kim. Computational screening of trillions of metal–organic frameworks for high-performance methane storage. *ACS Applied Materials & Interfaces*, 13(20):23647–23654, 2021.
- [12] Walter Kohn, Axel D Becke, and Robert G Parr. Density functional theory of electronic structure. *The journal of physical chemistry*, 100(31):12974–12980, 1996.

- [13] Martin Karplus and Gregory A Petsko. Molecular dynamics simulations in biology. *Nature*, 347(6294):631–639, 1990.
- [14] Li Shao, Jinrong Ma, Jesse L Prelesnik, Yicheng Zhou, Mary Nguyen, Mingfei Zhao, Samson A Jenekhe, Sergei V Kalinin, Andrew L Ferguson, Jim Pfaendtner, et al. Hierarchical materials from high information content macromolecular building blocks: construction, dynamic interventions, and prediction. *Chemical reviews*, 122(24):17397–17478, 2022.
- [15] Hilal Daglar and Seda Keskin. Recent advances, opportunities, and challenges in high-throughput computational screening of mofs for gas separations. *Coordination Chemistry Reviews*, 422:213470, 2020.
- [16] Kaylyn Torkelson, Nada Y Naser, Xin Qi, Zhiliang Li, Wenchao Yang, Karthik Pushpavanam, Chun-Long Chen, François Baneyx, and Jim Pfaendtner. Rational design of novel biomimetic sequence-defined polymers for mineralization applications. *Chemistry of Materials*, 36(2):786–794, 2024.
- [17] Mingfei Zhao, Shuai Zhang, Renyu Zheng, Sarah Alamdari, Christopher J Mundy, Jim Pfaendtner, Lilo D Pozzo, Chun-Long Chen, James J De Yoreo, and Andrew L Ferguson. Computational and experimental determination of the properties, structure, and stability of peptoid nanosheets and nanotubes. *Biomacromolecules*, 24(6):2618–2632, 2023.
- [18] Sakshi Yadav Schmid, Xiang Ma, Joshua A Hammons, Sebastian T Mergelsberg, Bradley S Harris, Thomas Ferron, Wenchao Yang, Wenhao Zhou, Renyu Zheng, Shuai Zhang, et al. Influence of peptoid sequence on the mechanisms and kinetics of 2d assembly. *ACS nano*, 18(4):3497–3508, 2024.
- [19] Jing Wei, Xuan Chu, Xiang-Yu Sun, Kun Xu, Hui-Xiong Deng, Jigen Chen, Zhongming Wei, and Ming Lei. Machine learning in materials science. *InfoMat*, 1(3):338–358, 2019.
- [20] Yi Luo, Saientan Bag, Orysia Zaremba, Adrian Cierpka, Jacopo Andreo, Stefan Wuttke, Pascal Friederich, and Manuel Tsotsalas. Mof synthesis prediction enabled by automatic data mining and machine learning. *Angewandte Chemie International Edition*, 61(19):e202200242, 2022.
- [21] Sanggyu Chong, Sangwon Lee, Baekjun Kim, and Jihan Kim. Applications of machine learning in metal-organic frameworks. *Coordination Chemistry Reviews*, 423:213487, 2020.
- [22] Zongsu Han, Yihao Yang, Joshua Rushlow, Jiatong Huo, Zhaoyi Liu, Yu-Chuan Hsu, Rujie Yin, Mengmeng Wang, Rongran Liang, Kun-Yu Wang, et al. Development of the design and synthesis of metal-organic frameworks (mofs)–from large scale attempts, functional oriented modifications, to artificial intelligence (ai) predictions. *Chemical Society Reviews*, 2025.
- [23] Debasis Banerjee, Cory M Simon, Anna M Plonka, Radha K Motkuri, Jian Liu, Xianyin Chen, Berend Smit, John B Parise, Maciej Haranczyk, and Praveen K Thallapally. Metal-organic framework with optimally selective xenon adsorption and separation. *Nature Communications*, 7(1):1–7, 2016.

- [24] Peyman Z Moghadam, Yongchul G Chung, and Randall Q Snurr. Progress toward the computational discovery of new metal–organic framework adsorbents for energy applications. *Nature Energy*, 9(2):121–133, 2024.
- [25] Yongchul G Chung, Emmanuel Haldoupis, Benjamin J Bucior, Maciej Haranczyk, Seulchan Lee, Hongda Zhang, Konstantinos D Vogiatzis, Marija Milisavljevic, Sanliang Ling, Jeffrey S Camp, et al. Advances, updates, and analytics for the computation-ready, experimental metal–organic framework database: Core mof 2019. *Journal of Chemical & Engineering Data*, 64(12):5985–5998, 2019.
- [26] Christopher E Wilmer, Michael Leaf, Chang Yeon Lee, Omar K Farha, Brad G Hauser, Joseph T Hupp, and Randall Q Snurr. Large-scale screening of hypothetical metal–organic frameworks. *Nature chemistry*, 4(2):83–89, 2012.
- [27] Ibrahim B Orhan, Hilal Daglar, Seda Keskin, Tu C Le, and Ravichandar Babarao. Prediction of o₂/n₂ selectivity in metal–organic frameworks via high-throughput computational screening and machine learning. *ACS Applied Materials & Interfaces*, 14(1):736–749, 2021.
- [28] Aditya Nandy, Chenru Duan, and Heather J Kulik. Using machine learning and data mining to leverage community knowledge for the engineering of stable metal–organic frameworks. *Journal of the American Chemical Society*, 143(42):17535–17547, 2021.
- [29] Benjamin J Bucior, N Scott Bobbitt, Timur Islamoglu, Subhadip Goswami, Arun Gopalan, Taner Yildirim, Omar K Farha, Neda Bagheri, and Randall Q Snurr. Energy-based descriptors to rapidly predict hydrogen storage in metal–organic frameworks. *Molecular Systems Design & Engineering*, 4(1):162–174, 2019.
- [30] Andrew S Rosen, Shaelyn M Iyer, Debmalya Ray, Zhenpeng Yao, Alan Aspuru-Guzik, Laura Gagliardi, Justin M Notestein, and Randall Q Snurr. Machine learning the quantum-chemical properties of metal–organic frameworks for accelerated materials discovery. *Matter*, 4(5):1578–1597, 2021.
- [31] Tian Xie and Jeffrey C Grossman. Crystal graph convolutional neural networks for an accurate and interpretable prediction of material properties. *Physical review letters*, 120(14):145301, 2018.
- [32] Yeonghun Kang, Hyunsoo Park, Berend Smit, and Jihan Kim. A multi-modal pre-training transformer for universal transfer learning in metal–organic frameworks. *Nature Machine Intelligence*, 5(3):309–318, 2023.
- [33] Hyunsoo Park, Yeonghun Kang, and Jihan Kim. Enhancing structure–property relationships in porous materials through transfer learning and cross-material few-shot learning. *ACS Applied Materials & Interfaces*, 15(48):56375–56385, 2023.
- [34] Zhonglin Cao, Rishikesh Magar, Yuyang Wang, and Amir Barati Farimani. Moformer: self-supervised transformer model for metal–organic framework property prediction. *Journal of the American Chemical Society*, 145(5):2958–2967, 2023.

- [35] Pin Chen, Rui Jiao, Jinyu Liu, Yang Liu, and Yutong Lu. Interpretable graph transformer network for predicting adsorption isotherms of metal–organic frameworks. *Journal of Chemical Information and Modeling*, 62(22):5446–5456, 2022.
- [36] Duc Duy Nguyen and Guo-Wei Wei. Agl-score: algebraic graph learning score for protein–ligand binding scoring, ranking, docking, and screening. *Journal of chemical information and modeling*, 59(7):3291–3304, 2019.
- [37] Dong Chen, Kaifu Gao, Duc Duy Nguyen, Xin Chen, Yi Jiang, Guo-Wei Wei, and Feng Pan. Algebraic graph-assisted bidirectional transformers for molecular property prediction. *Nature communications*, 12(1):3521, 2021.
- [38] Afra Zomorodian and Gunnar Carlsson. Computing persistent homology. In *Proceedings of the twentieth annual symposium on Computational geometry*, pages 347–356, 2004.
- [39] Zixuan Cang and Guo-Wei Wei. Integration of element specific persistent homology and machine learning for protein-ligand binding affinity prediction. *International journal for numerical methods in biomedical engineering*, 34(2):e2914, 2018.
- [40] Dong Chen, Jian Liu, Jie Wu, Guo-Wei Wei, Feng Pan, and Shing-Tung Yau. Path topology in molecular and materials sciences. *The journal of physical chemistry letters*, 14(4):954–964, 2023.
- [41] Rui Wang, Duc Duy Nguyen, and Guo-Wei Wei. Persistent spectral graph. *International journal for numerical methods in biomedical engineering*, 36(9):e3376, 2020.
- [42] Zixuan Cang and Guo-Wei Wei. Topologynet: Topology based deep convolutional and multi-task neural networks for biomolecular property predictions. *PLoS computational biology*, 13(7):e1005690, 2017.
- [43] Yi Jiang, Dong Chen, Xin Chen, Tangyi Li, Guo-Wei Wei, and Feng Pan. Topological representations of crystalline compounds for the machine-learning prediction of materials properties. *npj computational materials*, 7(1):28, 2021.
- [44] Dong Chen, Jian Liu, and Guo-Wei Wei. Multiscale topology-enabled structure-to-sequence transformer for protein–ligand interaction predictions. *Nature Machine Intelligence*, 6(7):799–810, 2024.
- [45] Duc Duy Nguyen, Zixuan Cang, Kedi Wu, Menglun Wang, Yin Cao, and Guo-Wei Wei. Mathematical deep learning for pose and binding affinity prediction and ranking in d3r grand challenges. *Journal of computer-aided molecular design*, 33:71–82, 2019.
- [46] Duc Duy Nguyen, Kaifu Gao, Menglun Wang, and Guo-Wei Wei. Mathdl: mathematical deep learning for d3r grand challenge 4. *Journal of computer-aided molecular design*, 34:131–147, 2020.
- [47] Rachel C Rohde, Kurtis M Carsch, Matthew N Dods, Henry ZH Jiang, Alexandra R McIsaac, Ryan A Klein, Hyunchul Kwon, Sarah L Karstens, Yang Wang, Adrian J Huang, et al. High-temperature carbon dioxide capture in a porous material with terminal zinc hydride sites. *Science*, 386(6723):814–819, 2024.

- [48] Herbert Edelsbrunner. *Geometry and topology for mesh generation*. Cambridge University Press, 2001.
- [49] Afra J Zomorodian. *Topology for computing*, volume 16. Cambridge university press, 2005.
- [50] Jean-Claude Hausmann et al. *On the Vietoris-Rips complexes and a cohomology theory for metric spaces*. Université de Genève-Section de mathématiques, 1994.
- [51] Robert W Ghrist. *Elementary applied topology*, volume 1. Createspace Seattle, 2014.
- [52] Herbert Edelsbrunner. Smooth surfaces for multi-scale shape representation. In *International conference on foundations of software technology and theoretical computer science*, pages 391–412. Springer, 1995.
- [53] Robert Ghrist. Barcodes: the persistent topology of data. *Bulletin of the American Mathematical Society*, 45(1):61–75, 2008.
- [54] Fabian Pedregosa, Gaël Varoquaux, Alexandre Gramfort, Vincent Michel, Bertrand Thirion, Olivier Grisel, Mathieu Blondel, Peter Prettenhofer, Ron Weiss, Vincent Dubourg, et al. Scikit-learn: Machine learning in python. *the Journal of machine Learning research*, 12:2825–2830, 2011.
- [55] Xiaoqi Wei and Guo-Wei Wei. Persistent topological laplacians—a survey. *arXiv preprint arXiv:2312.07563*, 2023.
- [56] Jian Liu, Dong Chen, Feng Pan, and Jie Wu. Neighborhood path complex for the quantitative analysis of the structure and stability of carboranes. *Journal of Computational Biophysics and Chemistry*, 22(04):503–511, 2023.
- [57] Jian Liu, Dong Chen, Jingyan Li, and Jie Wu. Neighborhood hypergraph model for topological data analysis. *Computational and Mathematical Biophysics*, 10(1):262–280, 2022.
- [58] Dimitry Kozlov. *Combinatorial algebraic topology*, volume 21. Springer Science & Business Media, 2007.
- [59] Li Shen, Jian Liu, and Guo-Wei Wei. Evolutionary khovanov homology. *AIMS Mathematics*, 9(9):26139–26165, 2024.